Chapter 3
Nonlinear Characterization of a Bistable Energy Harvester Dynamical System

Vinicius G. Lopes, João Victor L. L. Peterson and Americo Cunha Jr.

Abstract This chapter explores the nonlinear dynamics of a bistable piezo-magneto-elastic energy harvester with the objective of determining the influence of external force parameters on the system response. Time series, phase space trajectories, Poincaré maps and bifurcation diagrams are employed in order to reveal system dynamics complexity and nonlinear effects, such as chaos incidence and hysteresis.

3.1 Introduction

Technological advances of the last decades have brought a wide variety of new portable electronic devices (smart phones, remote and micro sensors, smart medical implants, etc) and, at the same time bring great facilities to everyday life, created a huge demand for autonomous sources of energy. In this context, the energy harvesting technologies have been seeing as a potential solution in scenarios where conventional power supplying may not be practical or even available.

Energy harvesting technologies are based on physical-chemical properties of special (energy harvesting) materials, which provides electrical potential in response to an external stimulus, such as light (photoelectric), heat (pyroelectric) or mechanical vibration (piezoelectric), among others. A popular and comprehensible example of application may be found in solar energy generation, where the photovoltaic panels, gathering the minor units called cells which contains the silicon-based photoelectric material, when exposed to the sunlight incidence, performs its conversion into the electrical output power.

V. G. Lopes · J. V. L. L. Peterson · A. Cunha Jr. (✉)
Universidade do Estado do Rio de Janeiro, Rio de Janeiro, Brazil
e-mail: americo@ime.uerj.br

V. G. Lopes
e-mail: vinicius.g.lopes@uerj.br

J. V. L. L. Peterson
e-mail: joao.peterson@uerj.br

M. Belhaq (ed.), *Topics in Nonlinear Mechanics and Physics*,
Springer Proceedings in Physics 228, https://doi.org/10.1007/978-981-13-9463-8_3

The piezoelectric energy harvesting systems have been widely discussed on recent works. An interesting aspect concerns into the shape versatility of such materials making them suitable for many design applications, as shown by [37], also contributing to diversify its application possibilities—a review on it is addressed in [43]. Among the most promising ones, some examples can be found in different knowledge areas, as in medicine for powering pacemakers [23], the electrical engineering and telecommunications, for industrial facilities [14] and Internet of Things (IoF) wireless devices power supplying [19]; in mechanics, as way for power recovering from friction losses on vehicle suspensions [1] or from skyscrapers oscillations [44] or even for damping structural vibrations [13, 40].

The first vibration energy harvesting systems proposed were based on linear configurations, as the cantilever beam layout shown on Fig. 3.1. The relative simplicity of this system motivates new analysis and layouts, for example, as seen in [30]. Although, as shown by Cottone et al. [7] and, in more recent papers [20, 21, 41, 42], nonlinear configurations, such as the bistable inverse pendulum depicted in Fig. 3.2, may present better power recovering performances, when compared to the linear counterparts.

The richness of such devices dynamics, combined with the new available improvements in numerical simulation tools and computing resources, have been propelling a wide variety of analysis considering different devices layouts, as seen in [10, 18, 34, 39] for composite and cantilever vibrating beams, or in [11, 15, 25, 26] for inverse pendulum layouts and new designs as those discussed in [5, 8, 16, 33, 45].

The external forcing influence over harvesters energetic performance and dynamic characteristics have also been widely investigated in [4, 29, 31, 35], which consider mixed harmonic and random noise forcing, and also in [3, 12], that explore the possibility of energy scavenging in a quasi-periodic regime from a delayed dynamics. The multidisciplinary character of the theme also motivates the extension of the discussion to the coupled electrical circuits, as seen on [2, 6, 24, 38].

The same nonlinearities responsible to improve the devices energetic performance, on the other hand, contributes to raise the systems dynamics complexity, even leading to chaotic and unstable responses for some operational configurations. In [27, 28, 36] the authors demonstrates the presence of hysteresis effects on the nonlinear dynamical response of a piezo-magneto-elastic energy harvesting system, that is associated to the co-existence of multiple solutions, for the same operational conditions depending on the external forcing parameters values. Such phenomena highlight the importance of a detailed investigation of the nonlinear dynamics of devices in order to improve the comprehension of its behavior and limitations.

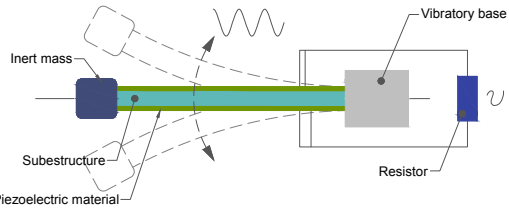

Fig. 3.1 Illustration of a linear vibration energy harvester

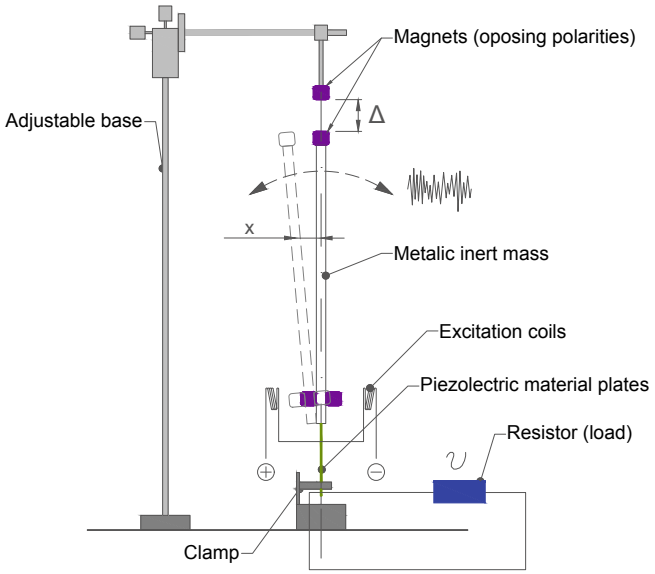

Fig. 3.2 Illustration of a nonlinear vibration energy harvester

In this sense, this chapter presents an analysis of the dynamics of a nonlinear bistable piezo-magneto-elastic energy harvesting system, aiming to investigate the influence of different harmonic forcing parameters on system output voltage. Numerical simulations reveals the effects of the amplitude and frequency excitation conditions on the chaos and regularity incidence on system electrical response. The bifurcation diagrams analysis allows to clearly identify the hysteresis phenomena and map those dynamics regions susceptible to chaos incidence. The voltage time series results sampled from such diagrams deepens the analysis of chaotic dynamics effects on the electrical output.

The rest of this chapter is organized as follows. The second section presents the energy harvesting system and its mathematical modeling. Next, in Sects. 3.3 and 3.4, the dynamical system is analyzed by time series and bifurcation diagrams, respectively. Final remarks close the text in the Sect. 3.5.

3.2 Bistable Energy Harvester

3.2.1 Physical System

The physical system of interest in this work is the piezo-magneto-elastic energy harvesting device depicted in Fig. 3.3. This electromechanical system consists of an elastic beam in vertical configuration, made of ferromagnetic material, with the

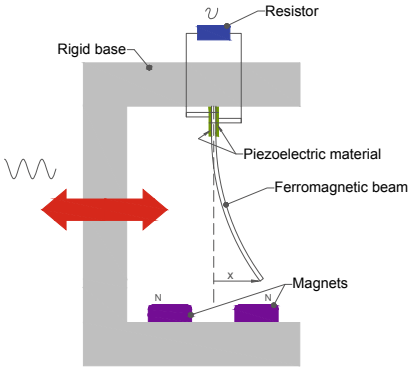

Fig. 3.3 Illustration of the piezo-magneto-elastic energy harvester

upper extreme clamped into a rigid base, and the bottom end moves freely. A pair of magnets is placed at the rigid base lower part. Two piezoelectric laminae are placed on beam's highest part, being also connected to a resistive circuit. The rigid base is periodically excited by an external source, which, together with the magnetic field generated by magnets, induces large amplitude vibrations in the beam. Once this movement is perceived by the piezoelectric laminae, the mechanical energy is converted into electrical power, which is dissipated in the resistor. This energy harvesting dispositive, proposed by Erturk et al. [9], is based on the classical magneto-elastic beam of Moon and Holmes [17, 32].

3.2.2 *Mathematical Model*

If the piezoelectric laminae and the electric circuit are not coupled to the system, the dynamic behavior of the beam is well approximated (for a limited frequency band) by its first mode shape, whose amplitude evolves according to a single degree-of-freedom Duffing oscillator [22]. However, once the piezoelectric transducer is attached to the beam, it starts to influence the system dynamic behavior so that piezoelectric interaction effect must be taken into account [9].

In this sense, [9] shows that the harvesting device dynamics can described by the following initial value problem

$$\ddot{x}(t) + 2\,\xi\,\dot{x}(t) - \frac{1}{2}x(t)\left(1 - x^2(t)\right) - \chi\,v(t) = f\,\cos\left(\Omega\,t\right), \tag{3.1}$$

$$\dot{v}(t) + \lambda\,v(t) + \kappa\,\dot{x}(t) = 0, \tag{3.2}$$

$$x(0) = x_0,\ \dot{x}(0) = \dot{x}_0,\ v(0) = v_0, \tag{3.3}$$

where t denotes time; x is the beam tip amplitude of oscillation; v is the voltage in the resistor; ξ is the damping ratio; f is the amplitude of the external force induced by the rigid base oscillation; Ω is the external excitation frequency; λ is a reciprocal time constant; the piezoelectric coupling terms are represented by χ, in the mechanical equation, and by κ in the electrical one; x_0 represents the beam edge initial position; $\dot{x}_0$ is the beam edge initial velocity; and v_0 denotes the initial voltage over the resistor. The upper dot is an abbreviation for time derivative. All parameters described above are dimensionless.

For all the simulations reported below, unless something is said on the contrary, the following dimensionless parameters are used: $\xi = 0.01$, $\kappa = 0.5$, $\chi = 0.05$, $\lambda = 0.05$, $\Omega = 0.8$. The standard initial conditions is $(x_0, \dot{x}_0, v_0) = (1, 0, 0)$. Different values of f are used, being indicated below. The dynamic is investigated for a temporal window defined by the interval $0 \leq t \leq 5000$.

3.3 Time Series Analysis

3.3.1 Effects of Excitation Amplitude

The voltage time series, analyzed for $0.019 \leq f \leq 0.275$, with amplitude increments of 0.032, are shown in Fig. 3.4. The steady state behavior is shown in the red window and, when pertinent, the transient behavior is depicted in a yellow box.

Figure 3.4a show the response of the system for excitation amplitude $f = 0.019$. The energy generated with such small excitation amplitude is minimal, and the response present regular behavior throughout the analyzed range. In Fig. 3.4b, as the forcing amplitude increases, the response assumes a larger amplitude. With $f = 0.083$ the response assumes a chaotic behavior, as can be seen in the yellow and red boxes. The voltage generated by the system increases. In Fig. 3.4d the dynamic presents regular steady state response starting from approximately 1000 time units, whereas it transient response is still chaotic. The amplitude of voltage output rises, to approximately 1 nondimensional volt, now that the energy input is considerably higher. The subsequent images Fig. (3.4e, f, g, h and i) present more or less the same response. All of them have wide amplitude range, between -1 and 1, and regular response at steady state, with little transient response.

In Fig. 3.5 it is possible to see a comparison between the chaotic attractor for $f = 0.083$, and the regular one, for $f = 0.115$. This figure also show the respective projections in the planes of displacement versus velocity, displacement versus voltage and velocity versus voltage, and corresponding Poincaré sections depicted by red dots. One can notice that a minimum change of the order of 0.032, that corresponds to 3.2% of the characteristic displacement used in the nondimensionalization, in the value of excitation amplitude can resolve in a totally different response. For $f = 0.083$, the dynamic presents chaotic behavior, trapped in the chaotic strange attractor, whereas for $f = 0.115$ the system resolve in a regular attractor. Once for the

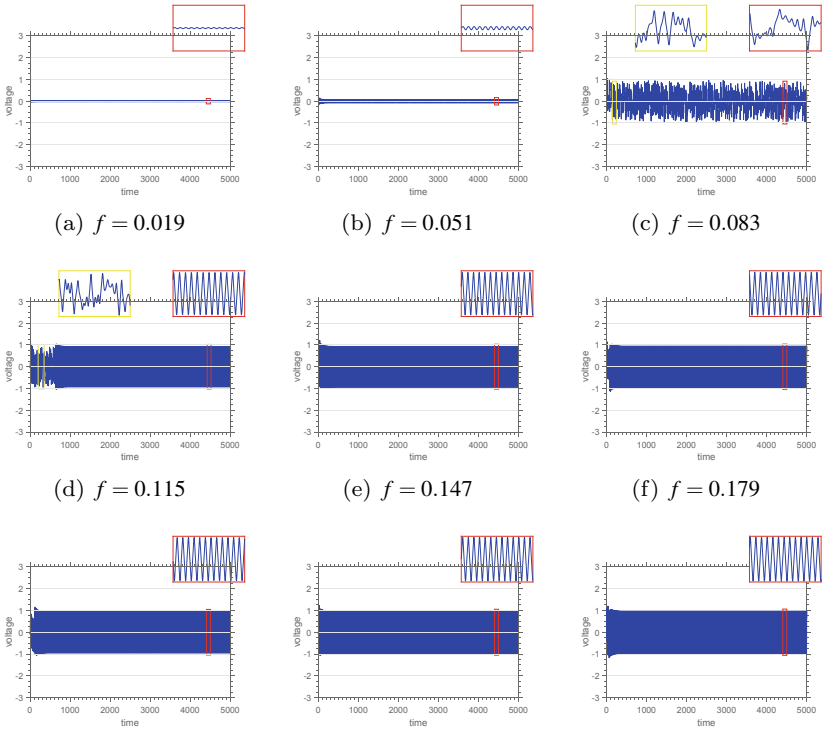

(a) $f = 0.019$ (b) $f = 0.051$ (c) $f = 0.083$

(d) $f = 0.115$ (e) $f = 0.147$ (f) $f = 0.179$

(g) $f = 0.211$ (h) $f = 0.243$ (i) $f = 0.275$

Fig. 3.4 Time series of voltage for $0.019 \leq f \leq 0.275$

chaotic configuration the system response presents non periodic pattern, its Poincaré section is represented by a large number of red dots not organized according to an invariant topological structure. The regular behavior has only one frequency, and thus, its Poincaré section has only one dot. The projections show that the regular attractor has higher energy output, characterized by its large amplitude in displacement.

A wide overview of the dynamics is best carried out by mapping the various attractors of the dynamical system. For this purpose the dynamics is integrated, for an excitation frequency $\Omega = 0.8$ and a total of 1200 different initial conditions, uniformly spaced in the region $-3 \leq x_0 \leq 3$, $-3 \leq \dot{x}_0 \leq 3$ and $v_0 = 0$, and the attractors corresponding to the steady-state of each case are identified. Projections of the identified attractors are shown in Fig. 3.6.

The attractors projections for forcing amplitude $f = 0.019$ are depicted on Fig. 3.6a. They are four in number, all with single period, being those depicted on magenta and cyan colors the more energetic orbits. For $f = 0.051$, which results are depicted on Fig. 3.6b, similar magenta and cyan basins are observed, as an expressive enlargement of blue and red basins shapes. Three regular orbits, depicted on brown, golden and green colors appears around those ones, reveling more energetic orbits which may be associated to the forcing amplitude increase. For $f = 0.083$,

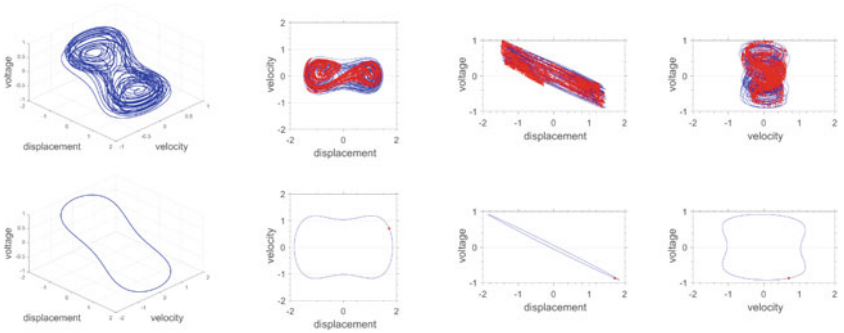

Fig. 3.5 Attractors in phase space for $f = 0.083$ (top) and $f = 0.115$ (bottom), phase space trajectories projections and corresponding Poincaré sections

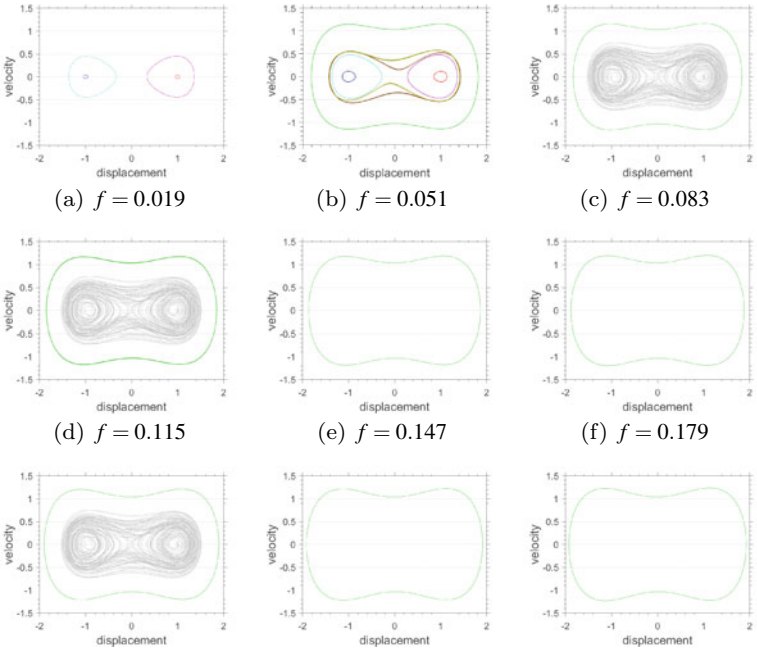

(a) $f = 0.019$ (b) $f = 0.051$ (c) $f = 0.083$

(d) $f = 0.115$ (e) $f = 0.147$ (f) $f = 0.179$

(g) $f = 0.211$ (h) $f = 0.243$ (i) $f = 0.275$

Fig. 3.6 Phase space trajectories projections for $0.019 \leq f \leq 0.275$ and $\Omega = 0.8$

on Fig. 3.6c, instead, the green orbit remains while the others disappears. A chaotic dynamics orbit, depicted on gray color, emerges corroborating the results observed on the phase attractor in Fig. 3.5, for the same model parameters. Similar results can be observed for $f = 0.211$, on Fig. 3.6g. For $f = 0.147$, $f = 0.179$, $f = 0.243$ and $f = 0.275$, which results are depicted, respectively, on Fig. 3.6e, f, h and i, a

single period orbit is observed, what reveals that, for such configurations, the system dynamics is regular.

3.3.2 *Effects of Excitation Frequency*

Now the effects of the excitation frequency over the system dynamics is explored trough attractors projections, calculated in a similar way as in the previous section, for $f = 0.083$, $f = 0.115$ and $0.1 \leq \Omega \leq 0.9$, and shown in Figs. 3.7 and 3.8, respectively.

The Fig. 3.7a, for $\Omega = 0.1$, reveals two low energy regular attractors with low amplitude orbits for beam displacement and velocity. Similar results can be observed for $f = 0.115$, on Fig. 3.8a, but with a chaotic attractor, on gray color. For $\Omega = 0.2$, on Fig. 3.7b, a clear narrowing of the basins shape is observed, as the chaos incidence, depicted on gray color, corresponding to larger amplitudes. The analysis of the attractors reveals a larger velocity range in regular response if compared with the previous case. Despite of the presence of a green regular attractor, no expressive changes are observed for $f = 0.115$ results, on Fig. 3.8b, in comparison with those for $f = 0.083$. For $\Omega = 0.3$, on Fig. 3.7c, the red basin prevails over the blue one;

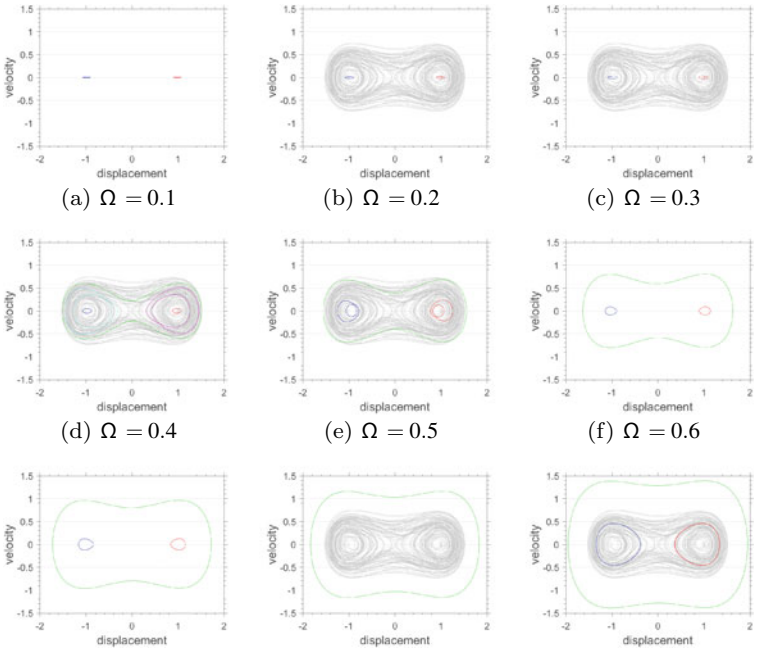

(a) $\Omega = 0.1$ (b) $\Omega = 0.2$ (c) $\Omega = 0.3$

(d) $\Omega = 0.4$ (e) $\Omega = 0.5$ (f) $\Omega = 0.6$

(g) $\Omega = 0.7$ (h) $\Omega = 0.8$ (i) $\Omega = 0.9$

Fig. 3.7 Phase space trajectories projections for $0.1 \leq \Omega \leq 0.9$ and $f = 0.083$

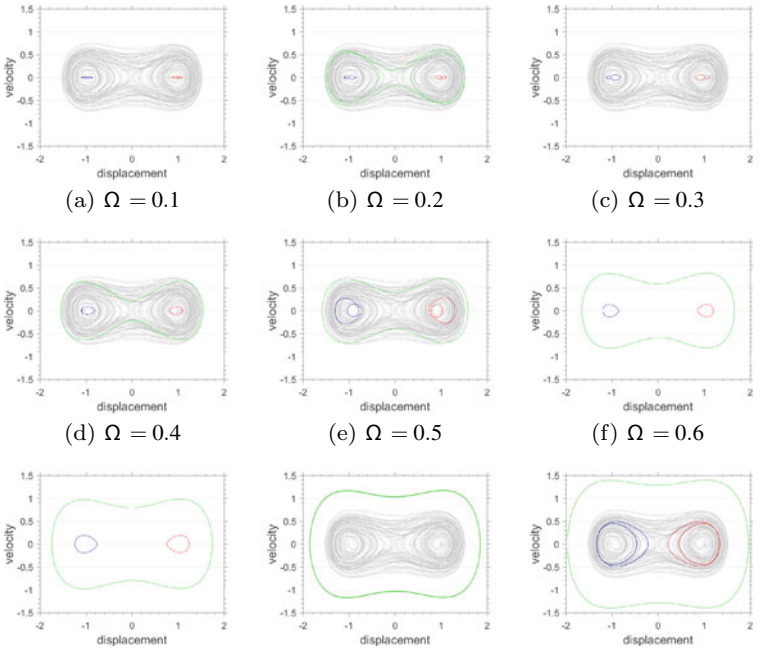

(a) $\Omega = 0.1$ (b) $\Omega = 0.2$ (c) $\Omega = 0.3$

(d) $\Omega = 0.4$ (e) $\Omega = 0.5$ (f) $\Omega = 0.6$

(g) $\Omega = 0.7$ (h) $\Omega = 0.8$ (i) $\Omega = 0.9$

Fig. 3.8 Phase space trajectories projections for $0.1 \leq \Omega \leq 0.9$ and $f = 0.115$

furthermore, the tendency of narrowing as the system moves away from the unforced system equilibrium points (presents in $(-1, 0)$ and $(1, 0)$) continues. The chaos still remains, as the attractors keep to increase in amplitude. A similar behavior is observed by considering $f = 0.115$, as show on Fig. 3.8c. For $\Omega = 0.4$, on Fig. 3.7d, one can note the predominance of the blue basin, although the red and blue basins are even more mixed. An expressive incidence of chaos is noted, despite of the presence of a new basin, depicted on green color, is noteworthy. The attractors show that such basin is more energetic due to a greater amplitude both in displacement and velocity. In addition, it is observed the emergency of two other basins, depicted on cyan and magenta colors, both with more energy than others, presenting two periods. For $f = 0.115$, on Fig. 3.8d, similar results can be observed except for the double period basins, which have disappeared. For $\Omega = 0.5$, in Fig. 3.7e, an expressive growth of the green basin occurs, along with the greater mix of peripheral regions, as the system gets closer to the resonance frequency. The attractors show the expansion of the green, blue and red basins and the inexistence of cyan and magenta ones. Also noteworthy is the transformation of the blue and red basins, now with two periods. No differences can be noted for $f = 0.115$ results, on Fig. 3.8e. The Fig. 3.7f, for $\Omega = 0.6$, shows the predominance of the green basin with blue and red islands. The attractors present a continuous growth of the green orbit, alongside with small growth of the blue and red orbits, which returned to present a single period and, in

counterpart with the previous case, there is absence of chaotic responses. Similar results are observed for $f = 0.115$, on Fig. 3.8f. For $\Omega = 0.7$, in Fig. 3.7g, a growth of the blue and red islands, as an increasing relevance of the green basin can be observed. The attractors continue to have more energetic orbits. Similar results can be observed for $f = 0.115$, depicted on Fig. 3.8g. In the system resonance frequency of $\Omega = 0.8$, depicted on Fig. 3.7h, the chaotic responses predominates along with the most energetic orbit, on green color. The attractors show that such orbit is the only regular one. Similar results are observed for $f = 0.115$, on Fig. 3.8h. Finally, for $\Omega = 0.9$, which results are depicted on Fig. 3.7i, the blue and red basins return subtly, still with presence of chaos. The attractors show the most energetic orbits. For $f = 0.115$, on Fig. 3.8i, despite of the similarities, the red and blue basins present double period orbits.

3.4 Bifurcation Analysis

The system bifurcation diagrams are built by sampling 1200 values for external excitation parameters from regularly spaced observation interval. Results are referred as forward and backward for an ascending and descending values sampling ordering, respectively. For each sampled amplitude, the dynamical system is integrated for a constant frequency. The first 90% of system response time series is neglected, as a way to avoid the transient response. From displacement, velocity and voltage results, the amplitude forward and backward bifurcation diagrams are obtained, according the chosen sampling ordering. A similar process can be carried out for frequency values, with constant amplitudes, leading to frequency forward and backward bifurcation diagrams. For ongoing results, typically, cool colors are reserved for forward results, while the warm colors scale depict the backward ones.

3.4.1 Influence of Excitation Amplitude

Regarding amplitude analysis, both forward and backward bifurcation diagrams are built for nine Ω values regularly sampled from $0.1 \leq \Omega \leq 0.9$, considering the amplitude sampling interval as $0.1 \leq f \leq 1.4$. The output voltage results are shown on Fig. 3.9.

The blurred regions depict chaotic dynamic on system response, for those on that output voltage may assume a wide range of different values. An overview of both, forward and backward bifurcation diagrams, points that the system is strongly sensitive to non-regular dynamics for the highest amplitude and lowest frequency values analysed. Some similar phenomena can be seen on the first portion of amplitude control interval on highest frequencies. From $\Omega = 0.5$ and higher frequency values, some expressive discrepancies are observed on voltage output by comparison

of forward and backward sampling orderings. This concerns to the nonlinear effects introduced by the pair of magnets on harvester, which are also responsible for the bistable configuration. For $\Omega = 0.6$ and 0.7, the system voltage response keeps regular for all tested amplitudes on the interval. A multiple period region appears for the last forcing amplitude values, after some slim band of chaotic dynamics. Similar formations are observed between the chaotic regions on the two highest frequencies analysed.

The Fig. 3.10 presents both forward and backward bifurcation diagrams for $\Omega = 0.2$ and 0.8 extracted from frequencies observation window overview in Fig. 3.9. In both cases, for $\Omega = 0.2$, the system presents chaotic dynamics about $0.260 \leq f \leq 0.270$. A pitchfork bifurcation revealed on forward diagram near $f = 0.23$ is hidden by system dynamics on backward, and reappears about $f = 0.27$, which highlights the system response dependence from the problem initial conditions. Discontinuous regions are also observed on the last portion of amplitudes interval, suggesting a

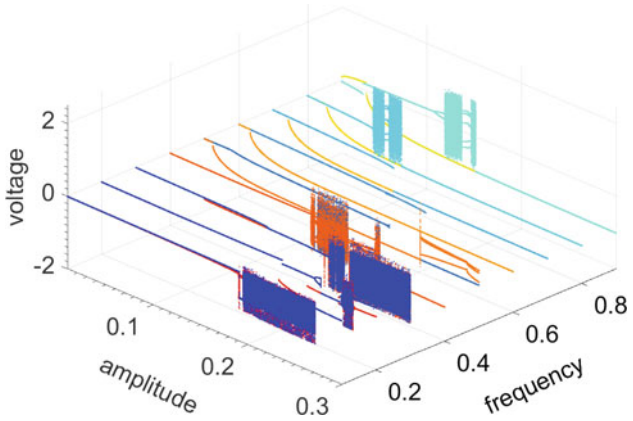

Fig. 3.9 Bifurcation diagram of voltage as function of excitation amplitude f, for several values of excitation frequency Ω

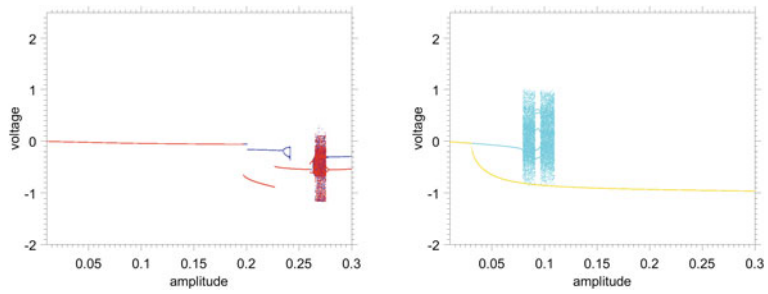

Fig. 3.10 Bifurcation diagrams for $\Omega = 0.2$ (left) and $\Omega = 0.8$ (right). Forward diagrams on blue colors and backward, on red and yellow

voltage behavior more independent of initial conditions, thus, reliable for the early amplitudes on this frequency. It is important to take account that such conclusions are true only for the model parameters defined. A similar analysis can be carried out for the amplitude bifurcation diagram for $\Omega = 0.8$. A pair of chaotic voltage

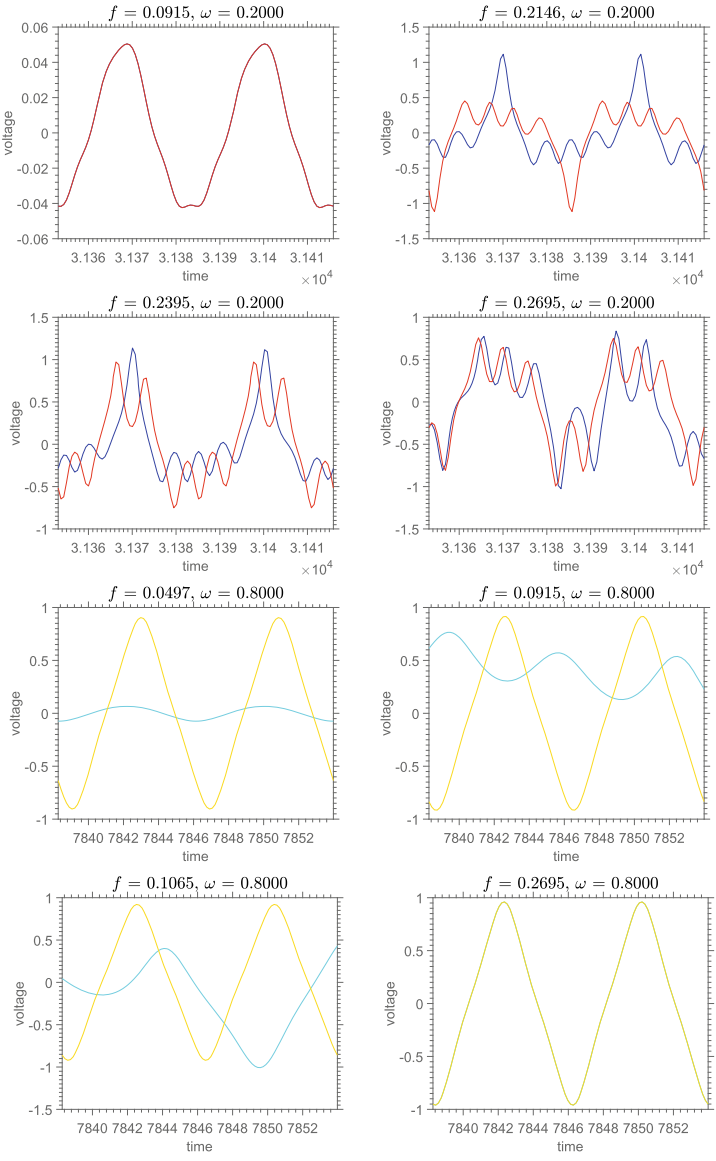

Fig. 3.11 Voltage time series for $\Omega = 0.2/\Omega = 0.8$ and several values of f. Forward diagrams on blue colors and backward, on red

bands can be seen on forward diagram for $0.07 \leq f \leq 0.08$ and $0.09 \leq f \leq 1.00$ filled by a richer multiple region. Now, instead, a strong regular dynamics region fills the middle and the last portions of the amplitude intervals both for forward and backward results.

Extending the previous discussion, Fig. 3.11 shows the voltage waveforms, obtained by sampling the system dynamics for specific forcing amplitude values taken from Fig. 3.10. For example, for $\Omega = 0.2$ and $f = 0.2146$, the harvester output voltage is regular, both on forward and backward diagrams, as seen before, besides the signal waveforms are quite distorted. For $f = 0.2695$ and the same excitation frequency, although both forward and backward waveforms have no period defined due to the chaotic motion.

3.4.2 *Influence of Excitation Frequency*

For the frequency analysis, the forward and backward diagrams are built for nine amplitude regularly sampled values from $0.019 \leq f \leq 0.275$, for $0.01 \leq \Omega \leq 1.4$ set as the frequency sampling interval. The Fig. 3.12 presents the harvester output voltage results.

For both forward and backward cases, the system reveals itself more susceptible to the chaos occurrence, when compared with those for amplitude analysis, depicted in Fig. 3.9. Despite of it, all diagrams present a common regular behavior in the middle portion of frequencies interval. The blurred regions became more evident for the last amplitude values in the observation windows, for which both low and high frequencies leads the system to chaos condition. Particularly, for $f \geq 0.179$, voltage results present multiple chaotic regions on backward diagrams, what emphasizes

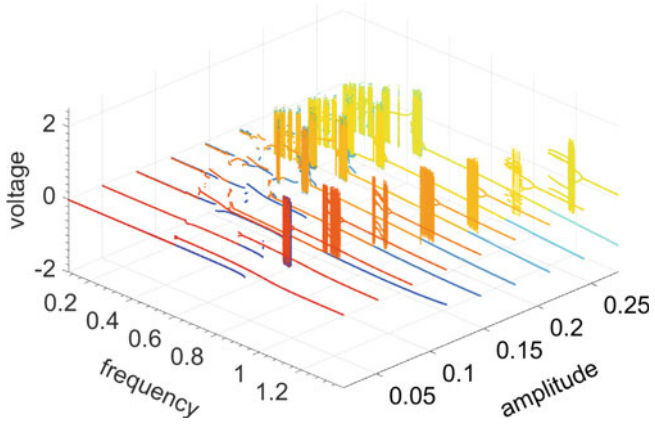

Fig. 3.12 Bifurcation diagram of voltage as function of excitation frequency Ω, for several values of excitation amplitude f

the influence of sampling ordering on explicit IPV solution. For higher amplitudes, multiple period regions and pitchfork bifurcations appear close to the chaotic regions, although it still means regular dynamics. A similar phenomena occurs on the early portion of frequencies interval $0.083 \leq f \leq 0.147$, where some discontinuities are also observed, both on forward and backward cases. By comparison with the same regions on higher amplitudes diagrams, the discontinuities, thus, may be inferred as a way to predict the chaos occurrence. For the lowest amplitude, system voltage results remains regular for all investigated frequencies. A small pitchfork bifurcation can still be noted on backward results about $f = 0.6$. This indicates that for different operation frequencies, a small forcing amplitude value may be interesting once it prevents chaotic dynamics.

The Fig. 3.13 presents the forward and backward diagrams for $f = 0.083$ and $f = 0.179$, sampled from amplitude observation window overview in Fig. 3.12. For $f = 0.083$, forward and backward methods reveals a similar dynamics profile regarding the chaos and regularity. The exception is confined to the region between $0.4 \leq f \leq 0.6$, where a pitchfork bifurcation on backward case gives rise to a discontinuity on forward one. The chaotic dynamics region about $\Omega = 0.8$ is small if compared with those observed for higher amplitude values, both on forward and backward results. For $f = 0.179$, as an overview of Fig. 3.12 suggestsc that the system presents a rich dynamics related to chaos occurrence. A strongly nonlinear region can be observed on the first middle of the frequencies interval, filled with large discontinuities region on its early portion. The system susceptibility to initial conditions for higher amplitudes, inducted by the sampling ordering, becomes more evident when forward and backward results are compared. A massive chaotic region rises around of $\Omega = 1.0$ on backward case, in contrast with regular dynamics on forward diagram on same region.

The system results investigation may be improved by sampling amplitude and frequency values from diagrams in Fig. 3.13, as shown by the voltage time series presented in Fig. 3.14. The voltage time series for $f = 0.179$ and $\Omega = 0.3786$, for example, highlights the importance of a deep investigation. System voltage waveforms presents a regular pattern, both on forward and backward diagrams. Although, the multiple period region distortion is more evident on backward case, once forward voltage waveform seems to preserve some characteristics of the harmonic forcing.

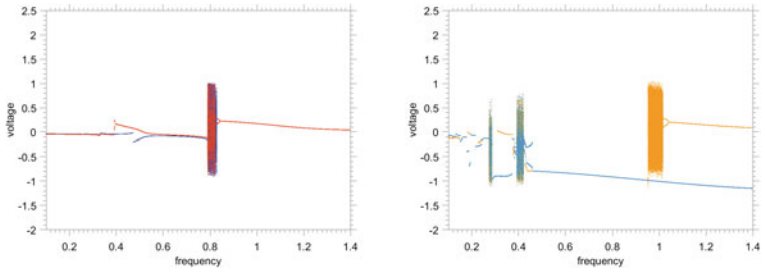

Fig. 3.13 Bifurcation diagrams for $f = 0.083$ (left) and $f = 0.179$ (right). Forward diagrams on blue colors and backward, on red

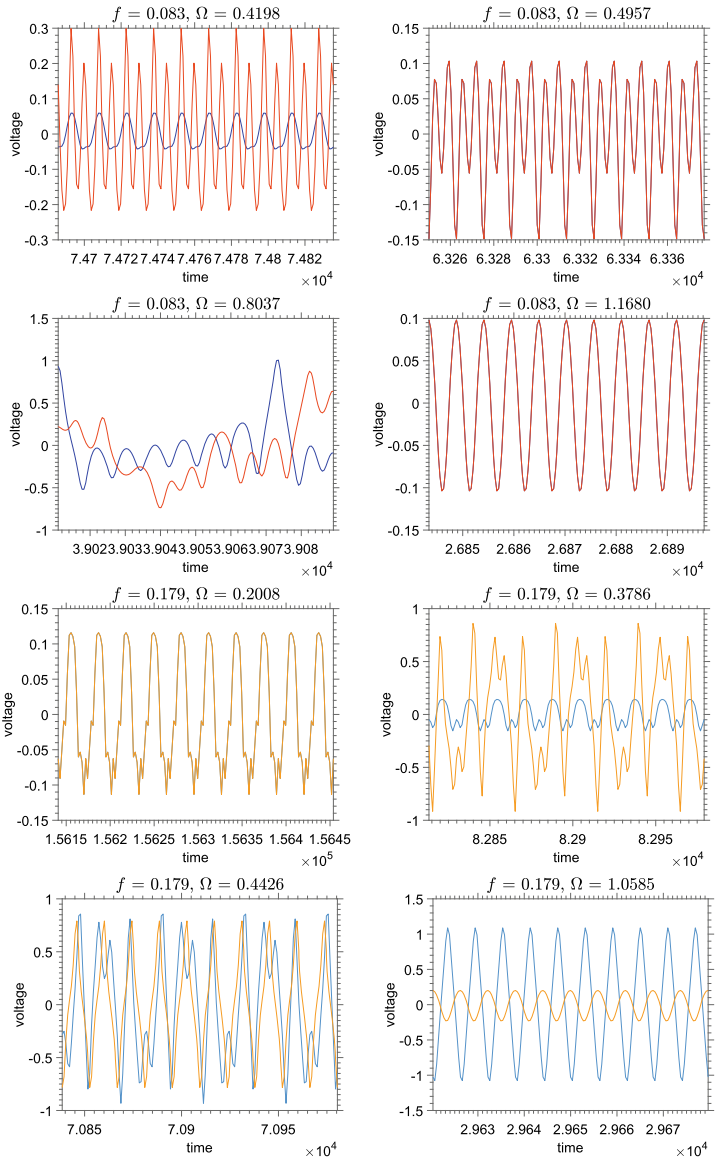

Fig. 3.14 Voltage time series for $f = 0.083/f = 0.179$ and several values of Ω. Forward diagrams on blue colors and backward, on red

In this sense, best results are observed for $f = 0.179$ with $\Omega = 1.0585$, where forward amplitudes overcomes backward one. The chaotic dynamics consequences is observed better for $f = 0.083$ with $\Omega = 0.8037$, in Fig. 3.14. A periodic behavior is not clearly seen on voltage waveforms, neither on forward or backward cases.

3.5 Concluding Remarks

This chapter presents a nonlinear dynamic analysis of a piezo-magneto-elastic energy harvesting system. Its nonlinear behavior is explored by time series, Poincaré maps, phase space trajectories and bifurcation diagrams. The voltage output time series and the phase attractors analysis allow to relate the length of the transient dynamics response to the external forcing frequency and amplitude parameters values. The same graphs also provide a way to link the magnitude of the harmonic forcing and the amount of output power. The bifurcation diagrams analysis reveals a hysteresis effects on the system dynamics which may be associated to the model nonlinearities, introduced by the pair of magnets placed on the rigid structure lower part, also responsible to the bistable configuration. The voltage time series sampled from such diagrams provides a detailed overview of the chaos incidence distortions on system output voltage waveforms.

Acknowledgements The authors acknowledge the support given to this research by the funding agencies Carlos Chagas Filho Research Foundation of Rio de Janeiro State (FAPERJ) under grants E-26/010.002.178/2015 and E-26/010.000.805/2018, and Coordenação de Aperfeiçoamento de Pessoal de Nível Superior–Brasil (CAPES)–Finance Code 001.

References

1. M.A.A. Abdelkareem, L. Xu, M.K.A. Ali, A. Elagouz, J. Mi, S. Guo, Y. Liu, L. Zuo, Vibration energy harvesting in automotive suspension system: a detailed review. Appl. Energy **229**, 672–699 (2018)
2. C.H.C.C. Basqueroto, F.R. Chavarette, S. da Silva, Analysis of bistable and chaotic piezoelectric energy harvesting device coupled with diode bridge rectifier. Int. J. Pure Appl. Math. **98**, 275–289 (2015)
3. M. Belhaq, M. Hamdi, Energy harvesting from quasi-periodic vibrations. Nonlinear Dyn. **86**, 2193–2205 (2016)
4. M. Borowiec, Energy harvesting of cantilever beam system with linear and nonlinear piezoelectric model. Eur. Phys. J. Spec. Top. **224**(14), 2771–2785 (2015)
5. S. Bradai, S. Naifar, C. Viehweger, O. Kanoun, G. Litak, Nonlinear analysis of an electrodynamic broadband energy harvester. Eur. Phys. J. Spec. Top. **224**(14), 2919–2927 (2015)
6. M.A. Clementino, R. Reginatto, S. da Silva, Modeling of piezoeletric energy harvesting considering the dependence of the rectifier circuit. J. Intell. Mater. Syst. Struct. **36**, 283–292 (2014)
7. F. Cottone, H. Vocca, L. Gammaitoni, Nonlinear energy harvesting. Phys. Rev. Lett. **102**, 080601 (2009)
8. H.L. Dai, Y.W. Yang, A. Abdelkefi, L. Wang, Nonlinear analysis and characteristics of inductive galloping energy harvesters. Commun. Nonlinear Sci. Numer. Simul. **59**, 580–591 (2018)
9. A. Erturk, J. Hoffmann, D.J. Inman, A piezomagnetoelastic structure for broadband vibration energy harvesting. Appl. Phys. Lett. **94**, 254102 (2009)
10. F.M. Foong, C.K. Thein, D. Yurchenko, On mechanical damping of cantilever beam-based electromagnetic resonators. Mech. Syst. Signal Process. **119**, 120–137 (2019)
11. M.I. Friswell, S.F. Ali, O. Bilgen, S. Adhikari, A.W. Lees, G. Litak, Non-linear piezoelectric vibration energy harvesting from a vertical cantilever beam with tip mass. J. Intell. Mater. Syst. Struct. **23**(13), 1505–1521 (2012)

12. Z. Ghouli, M. Hamdi, F. Lakrad, M. Belhaq, Quasiperiodic energy harvesting in a forced and delayed Duffing harvester device. J. Sound Vib. **407**, 271–285 (2017)
13. J.A.B. Gripp, L.C.S. Góes, O. Heuss, F. Scinocca, An adaptive piezoelectric vibration absorber enhanced by a negative capacitance applied to a shell structure. Smart Mater. Struct. **24**(12), 125017 (2015)
14. Z. Hadas, L. Janak, J. Smilek, Virtual prototypes of energy harvesting systems for industrial applications. Mech. Syst. Signal Process. **110**, 152–164 (2018)
15. E. Halvorsen, G. Litak, Statistics of a noise-driven elastic inverted pendulum. Eur. Phys. J. Appl. Phys. **70**(1), 10901 (2015)
16. P. Harris, G. Litak, J. Iwaniec, C.R. Bowen, Recurrence plot and recurrence quantification of the dynamic properties of cross-shaped laminated energy harvester. Appl. Mech. Mater. **849**, 95–105 (2016)
17. P. Holmes, A nonlinear oscillator with a strange attractor. Philos. Trans. R. Soc. A **292**, 429–448 (1979)
18. S. Ju, C. Ji, Impact-based piezoelectric vibration energy harvester. Appl. Energy **214**, 139–151 (2018)
19. P. Kamalinejad, C. Mahapatra, Z. Sheng, S. Mirabbasi, V.C.M. Leung, Y.L. Guan, Wireless energy harvesting for the internet of things. IEEE Commun. Mag. **53**, 102–108 (2015)
20. S. Kato, S. Ushiki, A. Masuda, A broadband energy harvester using leaf springs and stoppers with response stabilization control. J. Phys. Conf. Ser. **1052**, 012083 (2018)
21. J.M. Kluger, T.P. Sapsis, A.H. Slocum, Robust energy harvesting from walking vibrations by means of nonlinear cantilever beams. J. Sound Vib. **341**, 174–194 (2015)
22. I. Kovacic, M. Brennan, *The Duffing Equation: Nonlinear Oscillators and their Behavior* (Wiley, 2011)
23. A. Kumar, R. Kiran, V.S. Chauhan, R. Kumar, R. Vaish, Piezoelectric energy harvester for pacemaker application: a comparative study. Mater. Res. Express **5**, 075701 (2018)
24. Y. Liao, J. Liang, Unified modeling, analysis and comparison of piezoelectric vibration energy harvesters. Mech. Syst. Signal Process. **123**, 403–425 (2019)
25. G. Litak, M.I. Friswell, S. Adhikari, Regular and chaotic vibration in a piezoelectric energy harvester. Meccanica **51**(5), 1017–1025 (2016)
26. G. Litak, A. Rysak, M. Borowiec, M. Scheffler, J. Gier, Vertical beam modal response in a broadband energy harvester. Proc. Inst. Mech. Eng. Part K J. Multi-Body Dyn. 230 (2016)
27. V.G. Lopes, J.V.L.L. Peterson, A. Cunha Jr., Numerical study of parameters influence over the dynamics of a piezo-magneto-elastic energy harvesting device (In XXXVII Congresso Nacional de Matemática Aplicada e Computacional, São José dos Campos, Brazil, 2017)
28. V.G. Lopes, J.V.L.L. Peterson, A. Cunha Jr, On the nonlinear dynamics of a bi-stable piezoelectric energy harvesting device, in *24th ABCM International Congress of Mechanical Engineering (COBEM 2017)* (Curitiba, Brazil, 2017)
29. V.G. Lopes, J.V.L.L. Peterson, A. Cunha Jr, Analysis of the nonlinear dynamics of a bistable energy harvesting system with colored noise disturbances, in *Conference of Computational Interdisciplinary Science (CCIS 2019)* (2019)
30. Q. Lu, L. Liu, F. Scarpa, J. Leng, Y. Liu, A novel composite multi-layer piezoelectric energy harvester. Compos. Struct. **201**, 121–130 (2018)
31. W. Martens, U. von Wagner, G. Litak, Stationary response of nonlinear magneto-piezoelectric energy harvester systems under stochastic excitation. Eur. Phys. J. Spec. Top. **222**(7), 1665–1673 (2013)
32. F.C. Moon, P.J. Holmes, A magnetoelastic strange attractor. J. Sound Vib. **65**, 275–296 (1979)
33. R. Naseer, H.L. Dai, A. Abdelkefi, L. Wang, Piezomagnetoelastic energy harvesting from vortex-induced vibrations using monostable characteristics. Appl. Energy **203**, 142–153 (2017)
34. D. Pan, F. Dai, Design and analysis of a broadband vibratory energy harvester using bi-stable piezoelectric composite laminate. Energy Convers. Manag. **169**, 149–160 (2018)
35. T. Pereira, A. Paula, A. Fabro, M. Savi. Random effects in a nonlinear vibration-based piezoelectric energy harvesting system. Int. J. Bifurc. Chaos, (in press) (2019)

36. J.V.L.L. Peterson, V.G. Lopes, A. Cunha Jr., Dynamic analysis and characterization of a nonlinear bi-stable piezo-magneto-elastic energy harvester, in MATEC Web of Conferences vol. 241 (2018), p. 01001
37. D. Puspitarini, A. Suzianti, H. Al Rasyid, Designing a sustainable energy-harvesting stairway: determining product specifications using triz method. Procedia Soc. Behav. Sci. **216**, 938–947, in *Urban Planning and Architectural Design for Sustainable Development (UPADSD)* (2016)
38. T.M.P. Silva, M.A. Clementino, A. Erturk, C. de Marqui Jr., Equivalent electrical circuit framework for nonlinear and high quality factor piezoelectric structures. Mechatronics **54**, 133–143 (2018)
39. S. Stoykov, G. Litak, E. Manoach, Vibration energy harvesting by a timoshenko beam model and piezoelectric transducer. Eur. Phys. J. Spec. Top. **224**(14), 2755–2770 (2015)
40. M.A. Trindade, C.C. Pagani, L.P.R. Oliveira, Semi-modal active vibration control of plates using discrete piezoelectric modal filters. J. Sound Vib. **351**, 17–28 (2015)
41. K. Vijayan, M.I. Friswell, H. Haddad Khodaparast, S. Adhikari, Non-linear energy harvesting from coupled impacting beams. Int. J. Mech. Sci. **96**-**97**, 101–109 (2015)
42. C. Wang, Q. Zhang, W. Wang, J. Feng, A low-frequency, wideband quad-stable energy harvester using combined nonlinearity and frequency up-conversion by cantilever-surface contact. Mech. Syst. Signal Process. **112**, 305–318 (2018)
43. C. Wei, X. Jing, A comprehensive review on vibration energy harvesting: modelling and realization. Renew. Sustain. Energy Rev. **74**, 1–18 (2017)
44. X.D. Xie, Q. Wang, S.J. Wang, Energy harvesting from high-rise buildings by a piezoelectric harvester device. Energy **93**, 1345–1352 (2015)
45. Z. Zhou, W. Qin, W. Du, P. Zhu, Q. Liu, Improving energy harvesting from random excitation by nonlinear flexible bi-stable energy harvester with a variable potential energy function. Mech. Syst. Signal Process. **115**, 162–172 (2019)